Use of Micro Spoilers for Control of Finned Projectiles

John Dykes[1] and Mark Costello[2]
Georgia Institute of Technology, Atlanta, GA 30332-0420

Daniel L. Cler[3]
U.S. Army Research, Development and Engineering Command, Picatinny, NJ 07806

Robert Carson[4], and Robert Dillon[5]
U.S. Army Research, Development and Engineering Command Benét Laboratories, Watervliet, NY 19320

Relative to other air vehicles, the physical control mechanism on a smart projectile plays much more of a central role in the overall system design. Many different smart projectile control mechanisms have been created, including aerodynamic based mechanisms such as movable canards, propellant based mechanisms such as squibs, and inertia based mechanisms such as internal moving masses. The work reported here considers small micro spoilers located between rear fins to create aerodynamic force changes to enable projectile control. In particular, boundary layer shock interaction between the projectile body, fins, and micro spoilers provides a multiplicative effect on controllable forces and moments. A parametric study varying the micro spoiler configuration is conducted to examine the level of control authority possible for this control mechanism concept. Results indicate that relatively small micro spoilers located between fins generate substantial control authority that is capable of eliminating impact errors caused by muzzle jump, aerodynamic uncertainty, and atmospheric winds. These conclusions are based on CFD predictions of the effect of micro spoilers on air loads coupled to a rigid 6-degree-of-freedom projectile trajectory simulation.

Nomenclature

CFD	=	computational fluid dynamics
C_{NA}	=	normal force aerodynamic coefficient
C_{MQ}	=	pitch damping moment coefficient
C_{X0}	=	zero yaw aerodynamic axial force coefficient parallel to projectile motion
C_{Y0},C_{Z0}	=	aerodynamic trim coefficients perpendicular to projectile axis of symmetry
C_{LDD}	=	roll moment coefficient from fin cant
C_{YPA}	=	magnus force coefficient
C_{LP}	=	roll damping coefficient
D	=	projectile reference diameter
g	=	acceleration due to gravity (9.81 m/s^2)
I	=	projectile inertia matrix
K_P	=	controller proportional gain
K_I	=	controller integral gain
K_D	=	controller derivative gain
L,M,N	=	external moment components on the projectile body expressed in the projectile reference frame
L_{SA},M_{SA},N_{SA}	=	steady aerodynamic moment components on the projectile body expressed in the projectile reference frame

[1] Graduate Research Assistant, School of Mechanical Engineering, Member AIAA.
[2] Sikorsky Associate Professor, School of Aerospace Engineering, Associate Fellow AIAA.
[3] Senior Engineer, Weapons Technology Branch, Small & Medium Cal Division, RDAR-WSW-F.
[4] Mechanical Engineer, Electro-Mechanics & Controls Branch, RDAR-WSB-DA.
[5] Science Advisor, Director's Office, RDAR-WSB.

L_{UA},M_{UA},N_{UA} = unsteady aerodynamic moment components on the projectile body expressed in the projectile reference frame
L_C,M_C,N_C = micro spoiler moment components on the projectile body expressed in the projectile reference frame
m = mass of the projectile
p,q,r = components of the angular velocity vector of the projectile body expressed in the projectile reference frame
SoS = speed of sound for air
t_a = control system maneuver activation time
u,v,w = translation velocity components of the projectile center of mass expressed in the projectile reference frame
V = velocity magnitude of projectile center of mass
X,Y,Z = total external force components on the projectile body expressed in the projectile reference frame
X_G,Y_G,Z_G = gravitational force components on the projectile body expressed in the projectile reference frame
X_A,Y_A,Z_A = aerodynamic force components on the projectile body expressed in the projectile reference frame
X_C,Y_C,Z_C = micro spoiler force components on the projectile body expressed in the projectile reference frame
x,y,z = position vector components of the projectile body center of mass expressed in the inertial reference frame
α = total aerodynamic angle of attack
γ = projectile inertial trajectory error command angle
Γ = total projectile inertial trajectory error
δ = control system roll angle activation window
ρ = density of air
ϕ,θ,ψ = Euler roll, pitch and yaw angles

I. Introduction

DIRECT fire projectiles are fired by line-of-sight aiming from ground based platforms, helicopters, and fixed wing aircraft. A number of conditions can cause rounds to miss an intended target. These conditions include manufacturing inaccuracies of the gun tube, propellant, and projectile, along with variable atmospheric conditions, firing platform motion, and aiming errors. With the advent of low cost, small, rugged, micro-electro-mechanical systems, dramatic reduction in dispersion for direct fire projectiles equipped with a flight control system is possible. The control mechanisms must be capable of altering the trajectory of the projectile in such a way that impact point errors induced at launch and in flight can be corrected. At the same time, the control mechanism must be rugged to withstand high acceleration loads at launch, small so that payload space is not compromised, and inexpensive for cost considerations, as explained by Rogers[1]. Many different control mechanisms are being developed with the previous requirements in mind, but that all concepts essentially fall into three categories: aerodynamic load mechanisms, jet thrust mechanisms, and inertial load mechanisms. Examples of aerodynamic control mechanisms, including rotation of aerodynamic lifting surface appendages, deflection of the nose, and deflection of ram air to side ports. Examples of jet thrust control mechanisms include gas jet thrusters and explosive thrusters. Examples of inertial control mechanisms include internal translation of a control mass and internal rotation of an unbalanced part.

The control mechanism investigated in this paper falls into the category of an aerodynamic mechanism, where small micro spoilers are used to induce an aerodynamic force and moment perturbation on high-speed projectiles due to shock wave interaction between the fins, body, and micro spoilers. Massey[4-6] as well as Bell[7] considered protuberances on fin-body interactions of high-speed projectiles. Both computational and experimental analysis showed that significant force multiplication can exist by modifying the boundary layer shock interaction of the projectile fin and body. The devices used in these previous studies were relatively large (on the order of one third the fin height) and protruded beyond the boundary layer. Large and controllable aerodynamic load perturbations were noted. A similar physical control mechanism is considered here. A number of small micro spoilers are inserted between the rear fins of the projectile. The micro spoilers are activated in a coordinated fashion to generate maximal control authority. A set of parametric trade studies are conducted on micro spoiler configurations and its effects on control authority is determined. Furthermore, active control performance of a nominal micro spoiler configuration is presented to establish the promise of this projectile control mechanism. Results provided in this paper are based on flight dynamic simulation using a rigid body representation. Prediction of the effects of micros spoiler deflection on aerodynamic loads is produced using computational fluid dynamics analysis. Details on these models are given below, followed by presentation of results.

II. Projectile Dynamic Model

The non-linear trajectory simulation used in this study is a standard 6-degree-of-freedom model typically used in flight dynamic modeling of projectiles. These 6 degrees of freedom include three inertial components of the position vector and three standard Euler projectile orientation angles, referenced to an 'earth-fixed' inertial frame. The equations of motion are provided in Eqs. (1)-(4), as derived by McCoy[8] and Murphy[9].

$$\begin{Bmatrix}\dot{x}\\ \dot{y}\\ \dot{z}\end{Bmatrix}=\begin{bmatrix}c_\theta c_\psi & s_\phi s_\theta c_\psi - c_\phi s_\psi & c_\phi s_\theta c_\psi + s_\phi s_\psi\\ c_\theta s_\psi & s_\phi s_\theta s_\psi + c_\phi c_\psi & c_\phi s_\theta s_\psi - s_\phi c_\psi\\ -s_\theta & s_\phi c_\theta & c_\phi c_\theta\end{bmatrix}\begin{Bmatrix}u\\ v\\ w\end{Bmatrix} \tag{1}$$

$$\begin{Bmatrix}\dot{\phi}\\ \dot{\theta}\\ \dot{\psi}\end{Bmatrix}=\begin{bmatrix}1 & s_\phi t_\theta & c_\phi t_\theta\\ 0 & c_\phi & -s_\phi\\ 0 & s_\phi / c_\theta & c_\phi / c_\theta\end{bmatrix}\begin{Bmatrix}p\\ q\\ r\end{Bmatrix} \tag{2}$$

$$\begin{Bmatrix}\dot{u}\\ \dot{v}\\ \dot{w}\end{Bmatrix}=\begin{Bmatrix}X/m\\ Y/m\\ Z/m\end{Bmatrix}-\begin{bmatrix}0 & -r & q\\ r & 0 & -p\\ -q & p & 0\end{bmatrix}\begin{Bmatrix}u\\ v\\ w\end{Bmatrix} \tag{3}$$

$$\begin{Bmatrix}\dot{p}\\ \dot{q}\\ \dot{r}\end{Bmatrix}=[I]^{-1}\left[\begin{Bmatrix}L\\ M\\ N\end{Bmatrix}-\begin{bmatrix}0 & -r & q\\ r & 0 & -p\\ -q & p & 0\end{bmatrix}[I]\begin{Bmatrix}p\\ q\\ r\end{Bmatrix}\right] \tag{4}$$

In Eqs. (1) and (2), the standard shorthand notation for trigonometric functions is used: $s_\alpha = \sin(\alpha)$, $c_\alpha = \cos(\alpha)$, and $t_\alpha = \tan(\alpha)$. The forces appearing in Eq. (3) contain contributions from gravity (G), body aerodynamics (A), and micro spoiler control (C).

$$\begin{Bmatrix}X\\ Y\\ Z\end{Bmatrix}=\begin{Bmatrix}X_G\\ Y_G\\ Z_G\end{Bmatrix}+\begin{Bmatrix}X_A\\ Y_A\\ Z_A\end{Bmatrix}+\begin{Bmatrix}X_C\\ Y_C\\ Z_C\end{Bmatrix} \tag{5}$$

The dynamic equations are expressed in a body fixed reference frame, thus all forces acting on the body are expressed in the projectile reference frame. The force acting due to gravity is shown in Eq. (6).

$$\begin{Bmatrix}X_G\\ Y_G\\ Z_G\end{Bmatrix}=mg\begin{Bmatrix}-s_\theta\\ s_\phi c_\theta\\ c_\phi c_\theta\end{Bmatrix} \tag{6}$$

The body aerodynamic force acting at the center of pressure of the projectile is given by Eq. (7).

$$\begin{Bmatrix}X_A\\ Y_A\\ Z_A\end{Bmatrix}=-\frac{\pi}{8}\rho V^2 D^2\begin{Bmatrix}C_{X0}+C_{X2}(v^2+w^2)/V^2\\ C_{NA}v\ /V\\ C_{NA}w\ /V\end{Bmatrix} \tag{7}$$

The applied moments about the projectile mass center contains contributions from steady aerodynamics (SA), unsteady aerodynamics (UA), and the micro spoiler control (C).

$$\begin{Bmatrix} L \\ M \\ N \end{Bmatrix} = \begin{Bmatrix} L_{SA} \\ M_{SA} \\ N_{SA} \end{Bmatrix} + \begin{Bmatrix} L_{UA} \\ M_{UA} \\ N_{UA} \end{Bmatrix} + \begin{Bmatrix} L_C \\ M_C \\ N_C \end{Bmatrix} \tag{8}$$

The moment components due to steady aerodynamic forces and control forces are computed with a cross product between the distance vector from the mass center to the location of the specific force and the force itself. The unsteady body aerodynamic moment provides a damping source for projectile angular motion and is given by Eq. (9).

$$\begin{Bmatrix} L_{SA} \\ M_{SA} \\ N_{SA} \end{Bmatrix} = \frac{\pi}{8} \rho V^2 D^3 \begin{Bmatrix} C_{LDD} + \dfrac{pDC_{LP}}{2V} \\ \dfrac{qDC_{MQ}}{2V} \\ \dfrac{qDC_{MQ}}{2V} \end{Bmatrix} \tag{9}$$

The projectile mass, center of gravity, and inertial properties are all assumed to be constant throughout the duration of the flight. The center of pressure location and all aerodynamic coefficients depend on local Mach number and are computed during simulation using linear interpolation. The dynamic equations given by Eqs. (1)–(4) are numerically integrated forward in time using a fourth-order, fixed step Runge-Kutta algorithm. Costello and Anderson[8] present correlation of this dynamic model against range data for a fin stabilized projectile. The forces and moments generated by the micro spoilers are described below.

III. Micro Spoiler CFD Analysis

A. CFD Model

The grid utilizes a tetrahedral mesh in the far-field with structured prism mesh at the near-wall surfaces with a starting cell height of 0.003 mm. The grid consists of 2.2 million cells. The CFD solution was run using ANSYS Fluent® 6.3.26 on 16 processors on an IBM System x3650/x3550 cluster. The 3-D solution utilizes the density-based explicit steady-state double-precision solver. The fluid medium is modeled as ideal gas air with properties at standard sea-level atmospheric conditions. The k-omega SST turbulence model is used to model near-wall and far-field turbulence. The near-wall boundary-layer mesh is on the order of y-star equal to one. The k-omega SST turbulence model utilizes a blended approach that allows the near-wall effects to modeled directly with the grid without compromising far-field effects. This is done with a blending function that models the near-wall directly (or with a k-omega model if sufficient grid does not exist to model it directly with y-star above 1) and then models the far-field with a k-epsilon turbulence model. This is accomplished through the use of a blending function that gradually turns the k-omega model into a k-epsilon model in the far-field. The benefit to this type of turbulence model in high-speed flow is better prediction of boundary-layer interaction and separation as is the case with the current configuration. Second order discretization is utilized for the flow equations, turbulent kinetic energy, and specific dissipation rate. The solution was run until solution residuals were reduced three orders of magnitude.

A baseline validation case is constructed based on the geometry develop by Massey[1]. The geometry selected mimicked the configuration where a pin diameter of 0.2 inches and height of 0.5 inches is located 0.6 inches from the trailing edge of a tapered fin mounted on a flat plate. The fin is exposed to Mach 1.7 flow from a round jet in the experimental setup. The experimental results produced 6.61 lbs of net side force on the fin and the CFD prediction produced 8.39 lbs of net side force on the fin. The experimental force was determined by assigning areas to each of the 28 pressure taps on the pin side of the fin and then integrating to determine the force on that side of the fin. In addition, forces were likely not calculated on the sharp rear and front edges of the fin due to the fact no instrumentation was located here. How the force was determined for the lee-ward side of the fin was not documented in Massey's report as well. Because pressure data was not available on the lee-ward side of the fin, some experimental error could have resulted. In addition, the entire fin may not have been completely submerged in the Mach 1.7 flow stream as was the case for the CFD model. Overall, CFD results compared favorably to experimental results.

B. Flat Plate Fin Interaction Design of Experiments Model

In order to understand the key elements governing force and moment generation from the micro spoilers, a multi-variable designed experiment is constructed for the micro spoilers on a flat plate configuration. A series of 27 different CFD runs were performed with ANSYS Fluent® 12.0 to parametrically vary five different geometric parameters to develop a quadratic response model. All CFD runs were performed at Mach =1.7 and zero deg sideslip angle of the fin. The five geometric parameters included the spacing between the group of micro spoilers and the sidewall of the fin, the angle of the micro flaps relative to the flat plate, the length of the micro spoilers, the number of rows of flaps in the streamwise direction, and the number of columns of flaps in the spanwise direction. Fig. 1 shows the design of experiments results for the top seven contributors to a quadratic fit of the total force generated on the fin, flat plate and micro spoilers. Shown are the percentages of each model contributor relative to the total sum of squares for the quadratic model of total force. This allows relative comparison of the effects over the range of the model. As can be seen, the two largest effects are the device angle squared and the number of devices in the streamwise direction. The device angle was varied from 30.0 deg off of the flat plate facing forward, through 90.0 deg to 150.0 deg facing rearward. The peak force was generated at 90.0 deg to the flat plate surface with a sharp fall-off at 30.0 and 150.0 deg. In addition, the number of devices in the streamwise direction and spanwise direction had a strong effect as well, with the streamwise direction having a slightly stronger effect. This was likely due to a stronger interaction with the fin in the streamwise direction as the shock structures reflected off of the fin. In addition, as the device length increased, the total force increased. There were also a couple of smaller cross interactions between two effects as well as the spacing of the overall pattern from the fin wall squared. Information from the designed experiment was utilized to optimize the micro spoiler layout for application to the Army-Navy finner configuration.

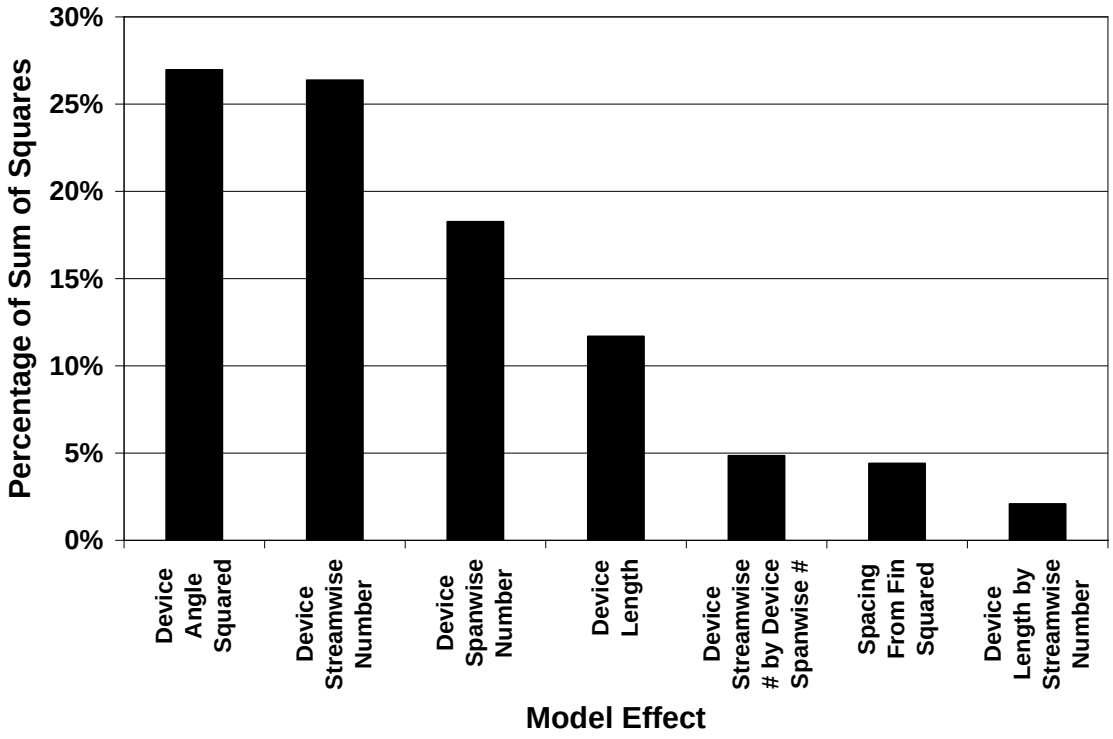

Figure 1. Design of Experiments results showing sum of squares from a quadratic fit of the total force generated on the fin, flat plate and micro spoilers.

C. Micro Spoiler Forces and Moments

Fig. 2 below shows the CFD model of the Army-Navy finner projectile with a single quadrant micro spoiler control mechanism. The model was run at zero angle of attack and zero angle of side slip form Mach 0.8 to Mach 4.0. A baseline configuration of the Army-Navy finner without micro spoilers was run at the same conditions. The micro spoiler configuration was optimized to produce the maximum force on the fin and body. With the configuration shown in Fig. 2, the forces are produced by increasing the pressure on two adjacent fins and projectile body between the fins. The forward two micro spoilers produce shock structures on the forward fin structure. The rear two micro spoilers are located inside the forward micro spoilers so they can receive unimpeded streamwise flow. These spoilers produce increase pressure near the rear of the fins and at the aft end of the projectile body. In addition to the micro flap configuration, Fig. 3 shows the pressure contours on the rear fin structure as a function of Mach number. As can be seen, the devices are fairly ineffective at subsonic conditions, but rather effective at supersonic conditions. Fig. 4 shows the forces and moments as a function of Mach number where delta forces and delta moments were calculated by subtracting the baseline configuration forces and moments. Above Mach 1.5, the devices become fairly effective. The pressures at the higher Mach numbers increase dramatically on the body and fins near the forward set of micro spoilers. The rear set of micro spoilers, though less effective, do offer some increase in pressures on the rear body and fin structure. From Mach 1.5 to 4.0, the micro spoiler total force and moment increase almost linearly as a function of Mach number. The micro spoilers are effective force multipliers by creating significant forces on both the fin and body through body-shock interactions.

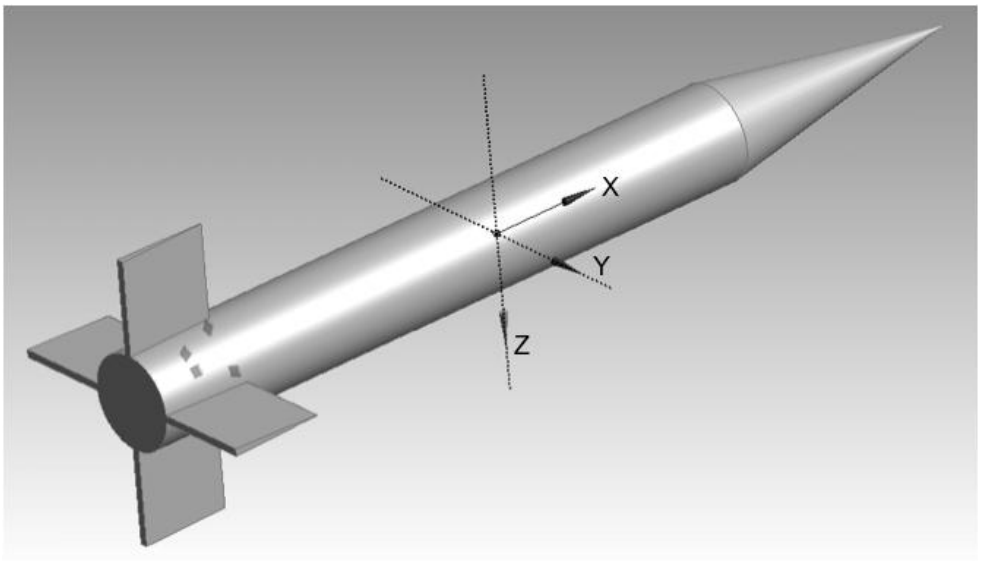

Figure 2. Schematic of an Army-Navy finner projectile possessing a 1-quadrant micro spoiler control mechanism configuration to be used in dynamic simulation.

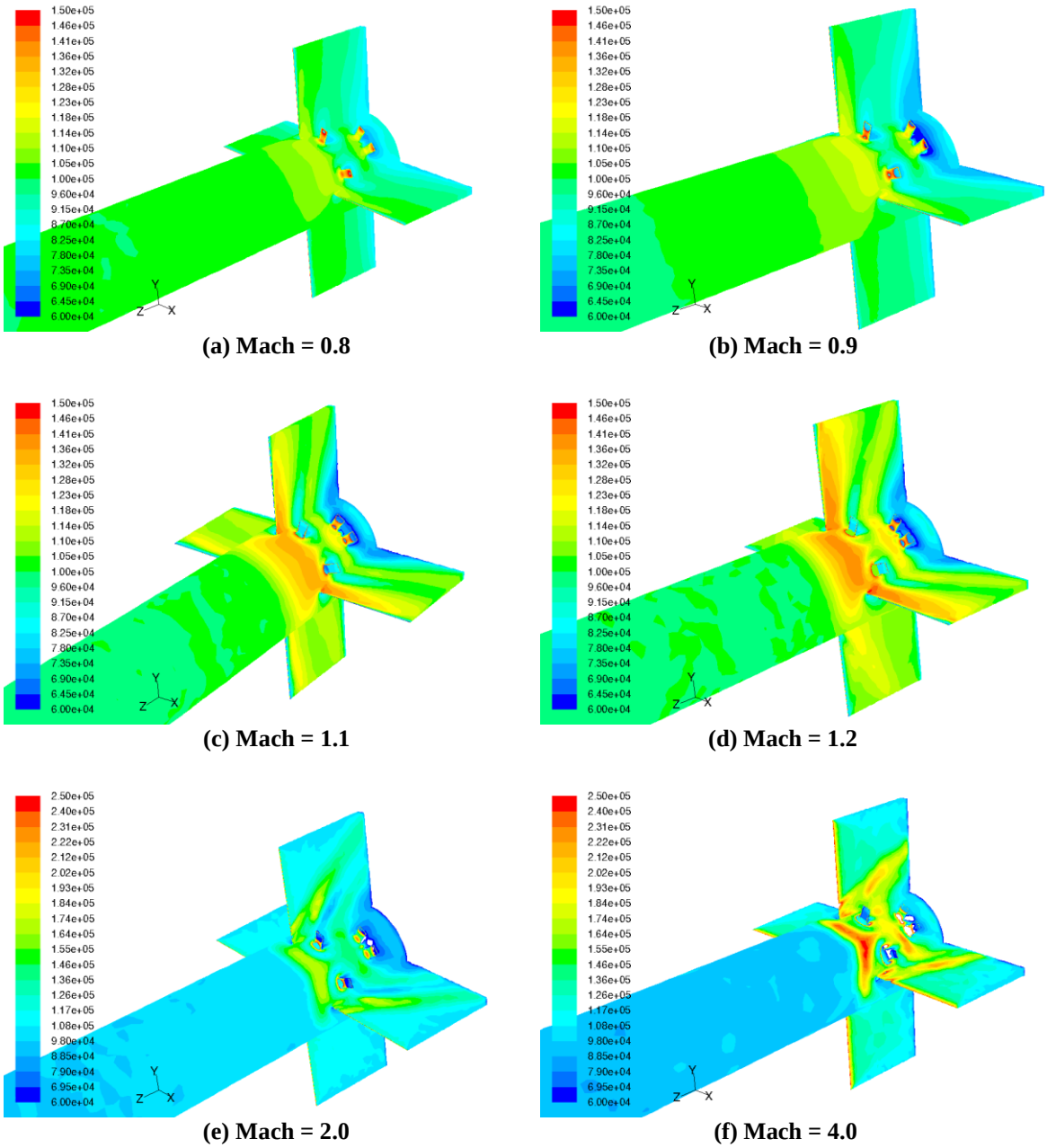

Figure 3. Static pressure contours (Pascals) of Army-Navy finner with micro spoilers deployed at (a) Mach = 0.8, (b) Mach = 0.9, (c) Mach = 1.1, (d) Mach = 1.2, (e) Mach = 2.0, and (f) Mach = 4.0.

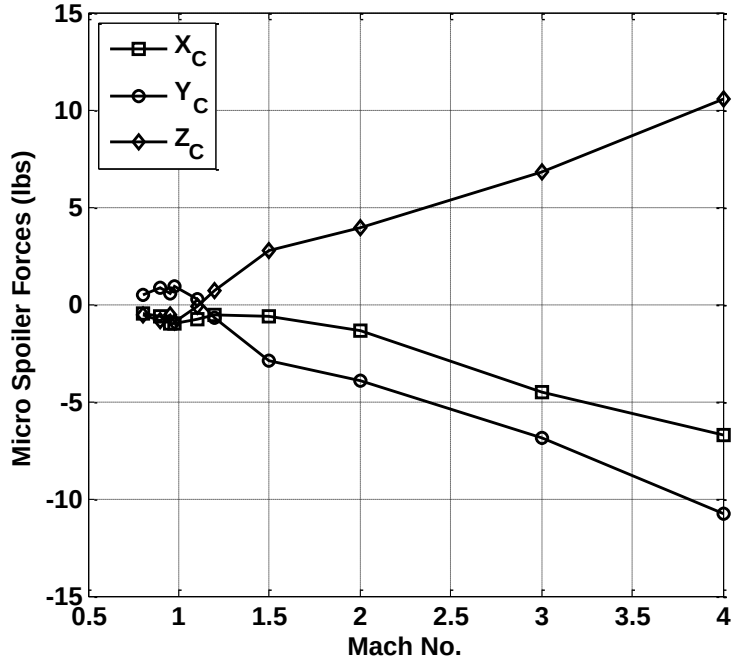

(a)

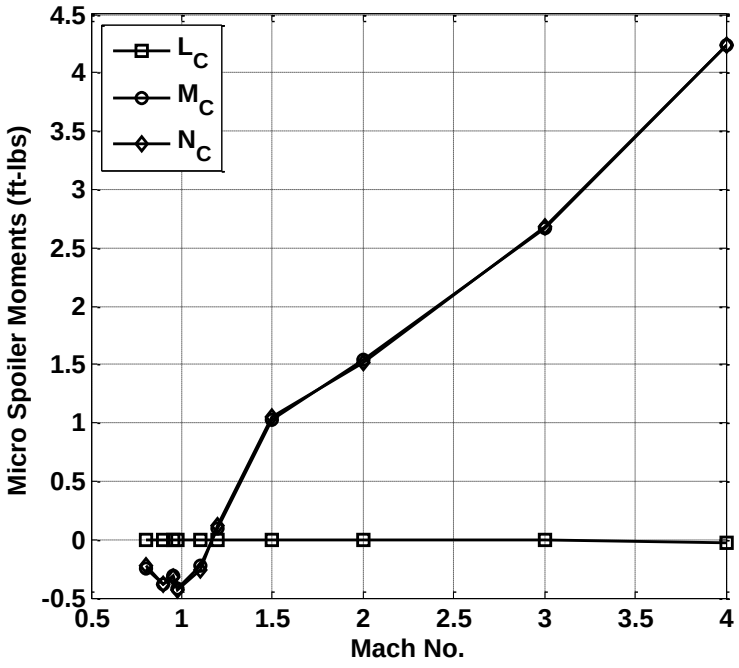

(b)

Figure 4. Mach number dependent micro spoiler (a) force and (b) moment perturbations acting about the projectile center of gravity for the reference frame shown in Fig. 2. This body reference frame is used in the trajectory simulations.

IV. Dynamic Flight Model Analysis

A. Description of Projectile

In order to examine the effectiveness of the micro spoiler control mechanism, trajectory results were generated for an example projectile. The Army-Navy finner shown above is used in this study as an example direct fire fin-stabilized projectile. From Dupuis[11], the projectile mass, diameter, mass center measured along the station line, roll inertia, and pitch inertia are 0.108851 slugs, 0.098425 ft, 0.4429 ft, 0.000142 slugs-ft^2, and 0.00728 slugs-ft^2, respectively. A fin cant angle of 0.25 deg was chosen to induce a moderate amount of roll rate. In all the following cases, the projectile is traveling through a standard atmosphere without atmospheric wind. A schematic of the basic projectile is shown below in Fig. 5.

B. Single Trajectory Results

Using the flight dynamics model previously described, a set of typical trajectory results are simulated. The projectile initial conditions are x = 0.0 ft, y = 0.0 ft, z = -10.0 ft, ϕ = 0.0 deg, θ = 1.02863 deg, ψ = 0.0 deg, u = 3357 ft/s, v = 0.0 ft/s, w = 0.0 ft/s, q = 0.0 rad/s, and r = 0.0 rad/s. A 4-quadrant micro spoiler configuration is used where a single micro spoiler is located between each fin. This is different than the CFD model where only one quadrant was deflected. However, it is likely only one quadrant will deflect at a time with the dynamic flight model, hence the static CFD model is a good approximately of dynamic flight model. Each fin on the projectile is 30.0 mm by 30.0 mm. Each of the four micro spoilers in a given quadrant is 3.0 mm wide and approximately 4.5 mm tall. The deflection angle between the micro spoiler and the projectile body is 90.0 deg. The two forward micro spoilers are 20.0 deg roll angle off of the nearest fin and the two rear micro spoilers are 40.0 deg roll off of the near fin. The forward micro spoilers are 25.0 mm from the rear of the projectile and the rear micro spoilers are 13.0 mm from the rear of the projectile.

Shown in Fig. 6, a simple flight control system is used to compute proper micro spoiler activation to execute a left turn. Control authority of the system is significantly affected by activation time t_a, command turn angle γ, and roll angle activation window δ. For this example trajectory, the maneuver activation time is set to 1.0 sec while the roll angle activation window is set to 60.0 deg.

Figs. 7-16 compare single trajectory results for uncontrolled and full left controlled projectiles. Fig. 7 shows that for a range of 3.0 km the controlled projectile was observed to deflect 161.3 m. Fig. 8 shows that minor differences in altitude between controlled and uncontrolled projectiles are experienced. Figs. 9 and 10 show that activating the control mechanism does introduce oscillatory motion in Euler pitch and yaw angles but dampens out considerably throughout the remainder of flight. Note that while the pitch angle does follow the uncontrolled pitch angle, the yaw angle diverges from the uncontrolled case from nearly 0.0 deg to -9.134 deg. Fig. 11 shows that the roll rate is also reduced by approximately 10.0 rad/s after activation. Figs. 12 and 13 show that maximal pitch and yaw rates never exceed 4.0 rad/s. In Fig. 14 the projectile total aerodynamic angle of attack experiences oscillations immediately after control activation to a maximum angle of 5.453 deg but quickly dampens down to below 2.0 deg in just over 1.0 sec of activation but not by a significant amount. Fig. 15 shows that the total velocity for the controlled projectile is reduced from the uncontrolled case. Fig. 16 shows that micro spoiler total force and moment perturbations in a body-fixed frame are successively roll activated with decreasing magnitude from 3.539 lbs and 1.215 ft-lbs as the projectile decelerates.

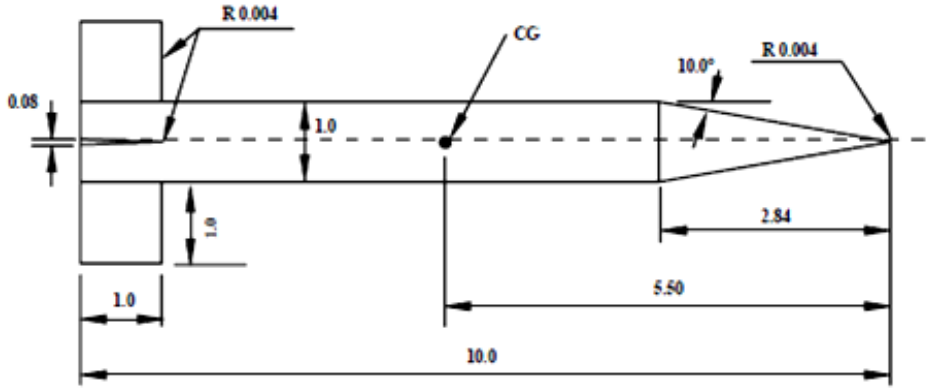

Figure 5. Army-Navy finner Geometry (all dimensions in calibers, 1 caliber = 30 mm).

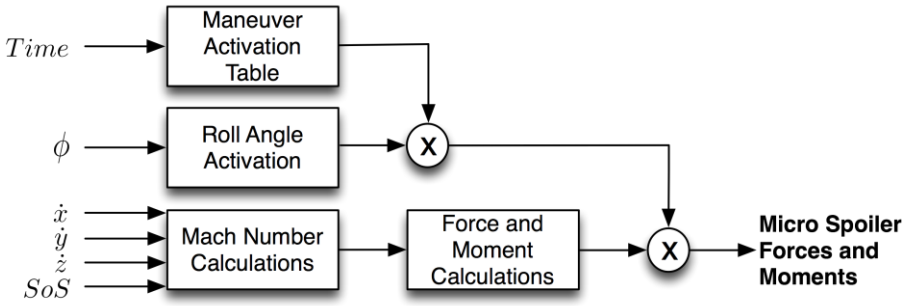

Figure 6. Block diagram modeling of micro spoiler forces and moments.

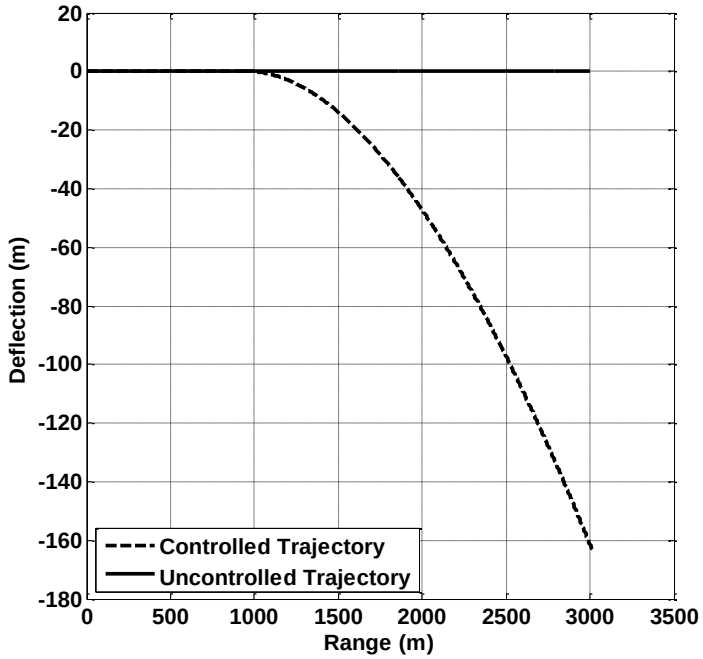

Figure 7. Deflection vs Range.

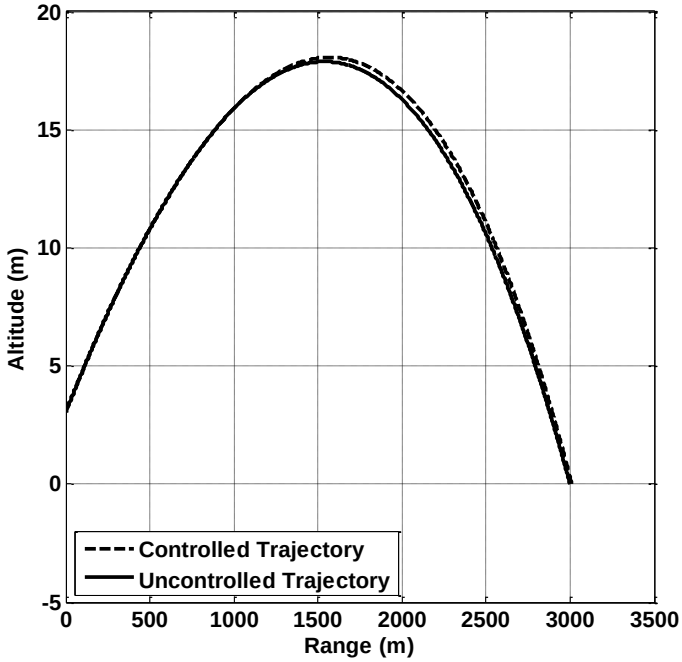

Figure 8. Altitude vs Range.

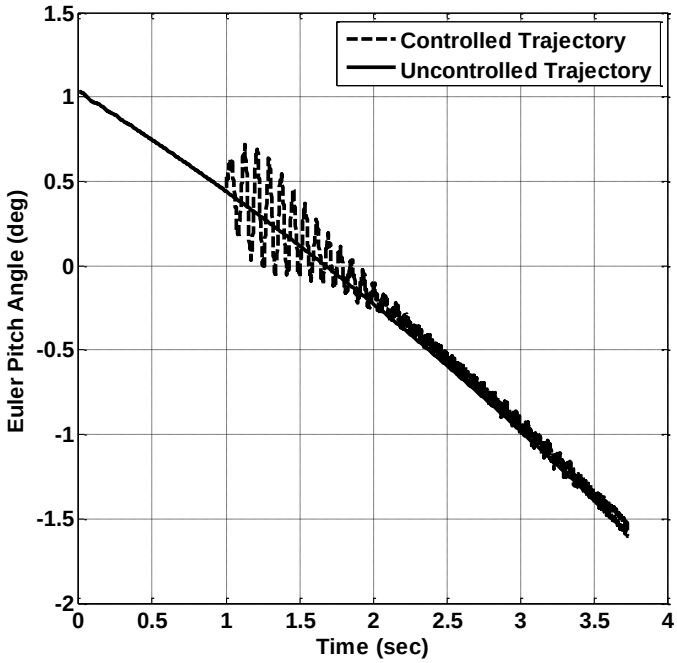

Figure 9. Pitch Angle vs Time.

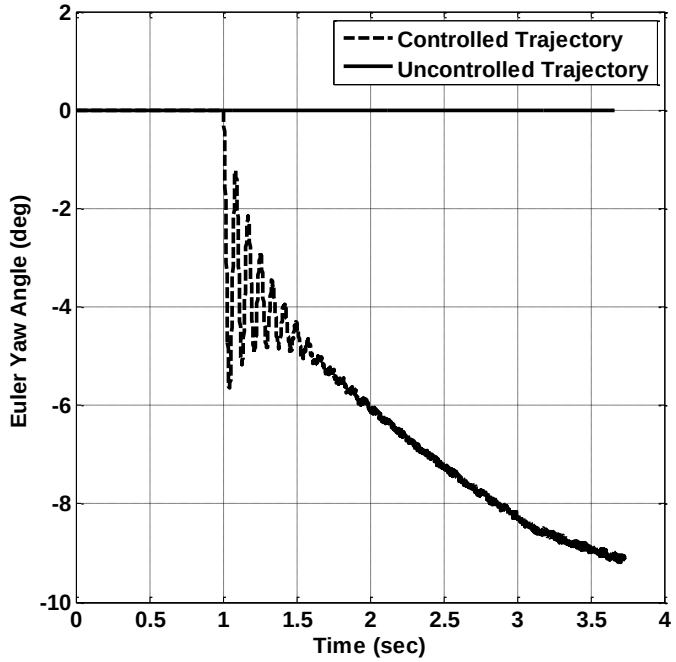

Figure 10. Yaw Angle vs Time.

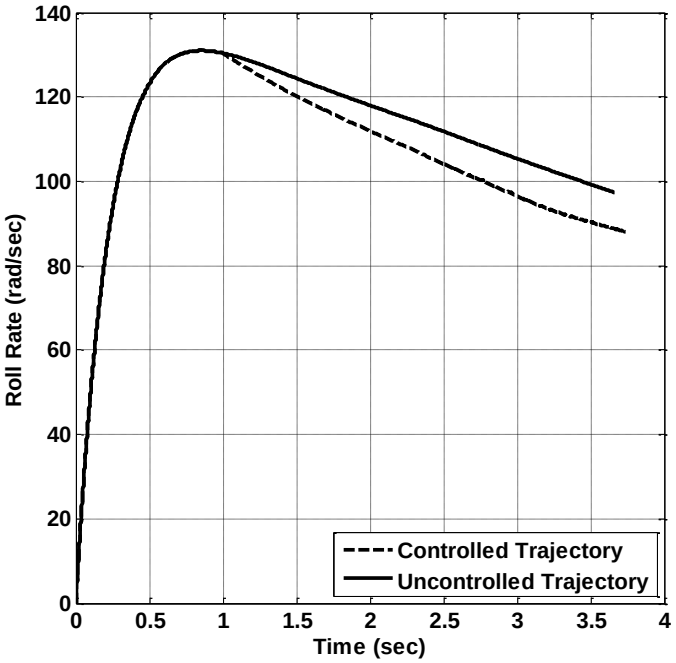

Figure 11. Roll Rate vs Time.

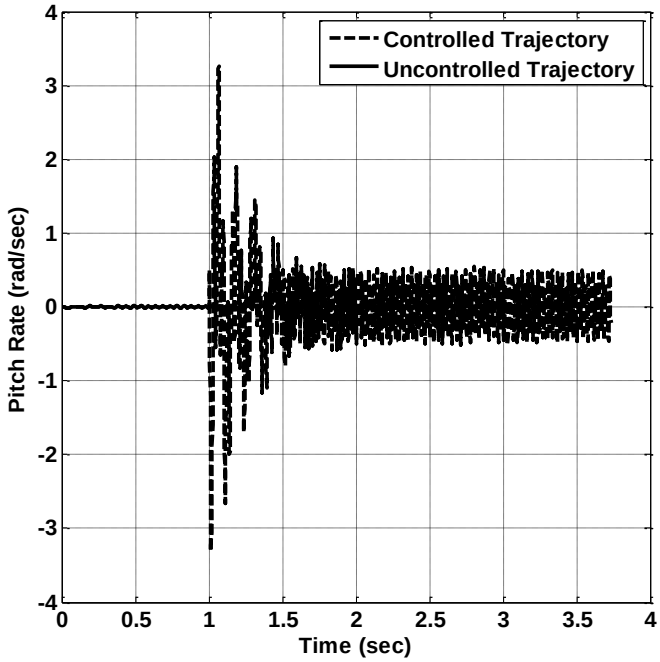

Figure 12. Pitch Rate vs Time.

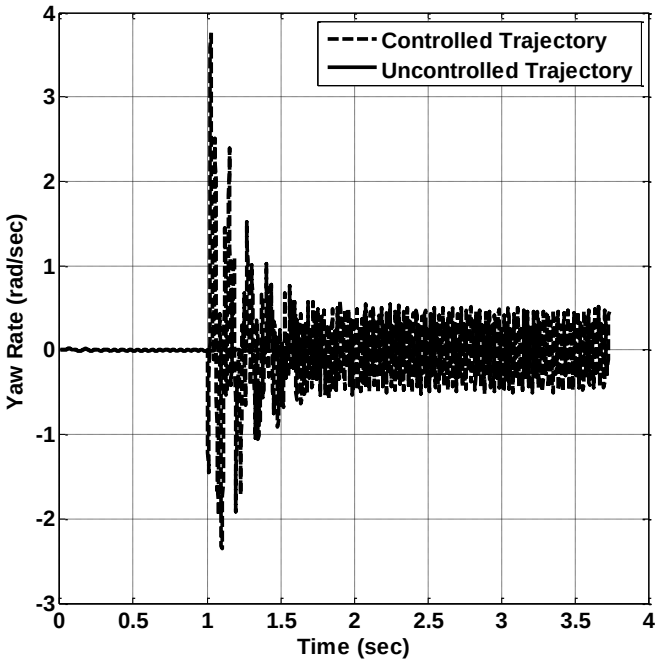

Figure 13. Yaw Rate vs Time.

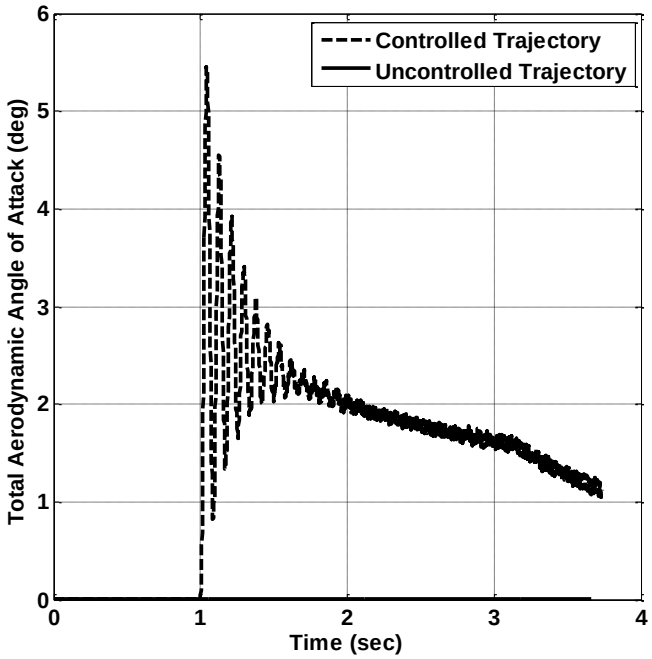

Figure 14. Angle of Attack vs Time.

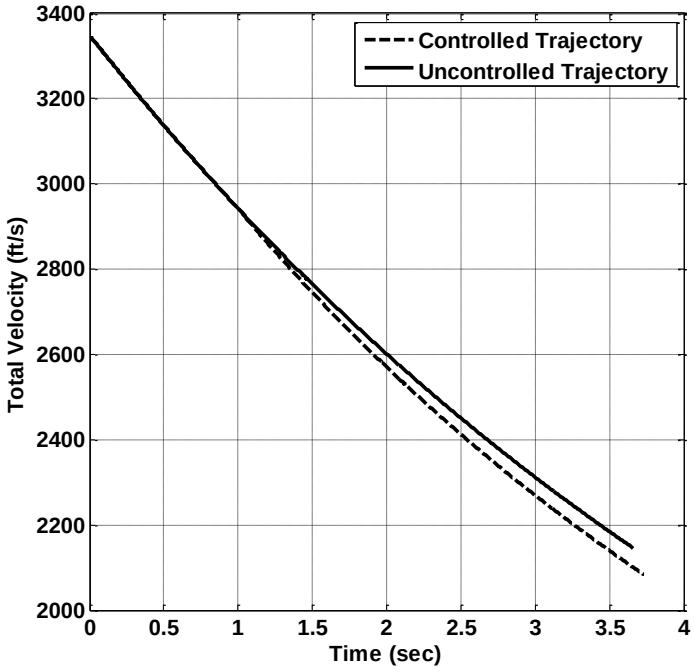

Figure 15. Total Velocity vs Time.

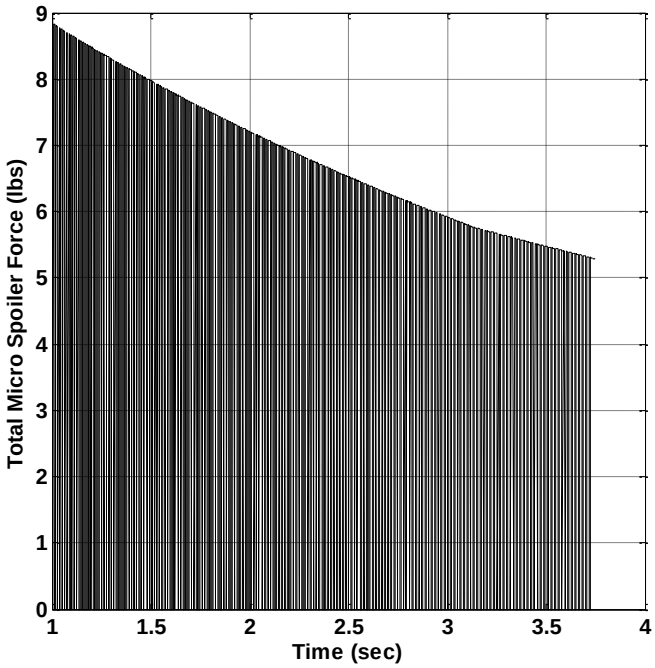

(a)

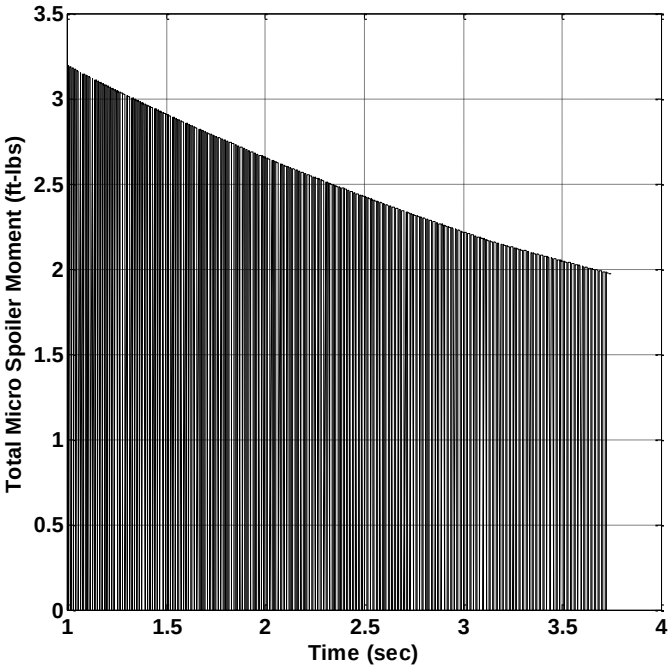

(b)

Figure 16. (a) Total Micro Spoiler Force Perturbations vs Time, and (b) Total Micro Spoiler Moment Perturbations vs Time after controller activation.

C. Control Authority Parametric Trade Study

Several parametric trade studies were computed to examine the control authority of the micro spoiler mechanism on the basic finner projectile, direct-fired to a range of 3.0 km. In all of the following trade studies the nominal projectile initial conditions are x = 0.0 ft, y = 0.0 ft, z = -10.0 ft, ϕ = 0.0 deg, θ = 1.03 deg, ψ = 0.0 deg, u = 3357 ft/s, v = 0.0 ft/s, w = 0.0 ft/s, q = 0.0 rad/s, and r = 0.0 rad/s. Also, nominal conditions for the control system parameters are set to t_a = 1.0 sec and δ = 60.0 deg, where γ is spanned from 0.0 to 360.0 deg in increments of 5.0 deg to produce a complete control authority footprint, as shown in Fig. 17. Trade studies include variation of control mechanism configuration, activation time, launch velocity, and roll angle activation window and are summarized in Figs. 18-21.

Fig. 18 shows that control authority linearly increases with variation of mechanism. CS1, CS2, CS3, and CS4 represent the number of micro spoiler control mechanisms implemented between the projectile fins (from 1 up to 4 quadrants). Fig. 19 shows that increasing the roll angle activation window has a positive effect on control authority but reaches a point of diminishing returns beyond 110.0 deg. In Fig. 20, increasing muzzle launch velocity is observed to have a positive effect on control authority; however, consideration must be given to the minimum value of this parameter to ensure that the projectile is exposed to supersonic conditions for the entirety of flight. Otherwise, the micro spoiler mechanisms will not properly function. Fig. 21 shows that delaying controller activation time has a negative effect on control authority, as expected.

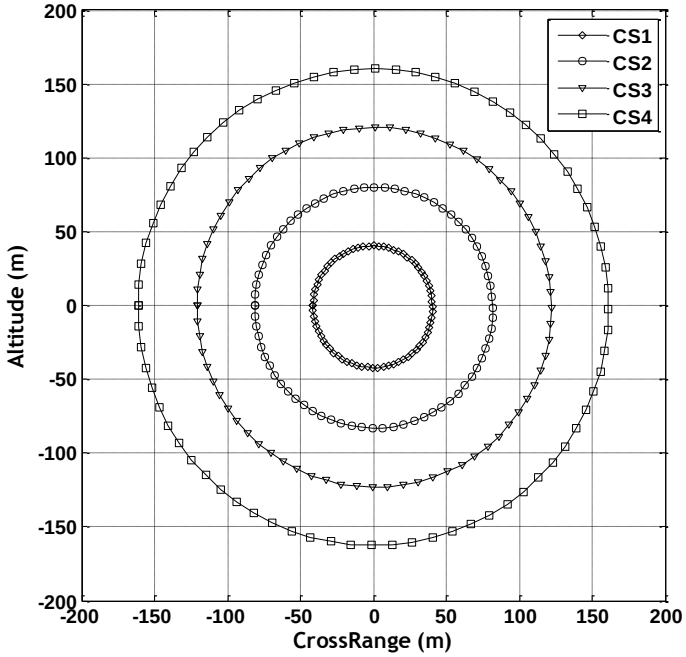

Figure 17. Full control authority dispersion map for variation in control system (CS) quadrant configuration at an impact range of 3.0 km with nominal conditions: t_a = 1.0 sec, δ = 60°, and Ma_i = 3.0.

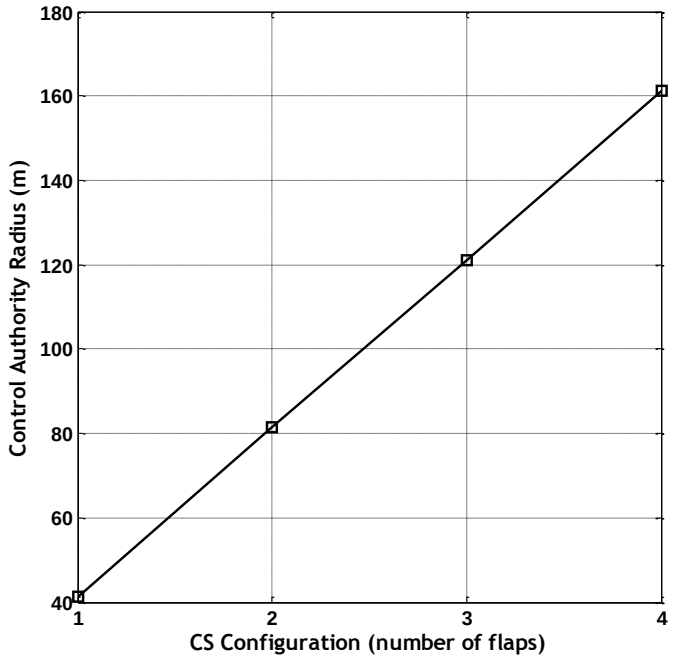

Figure 18. Trade study: effect of varied control system (CS) quadrant configuration on full control authority with nominal conditions: t_a = 1.0 sec, δ = 60°, and Ma_i = 3.0.

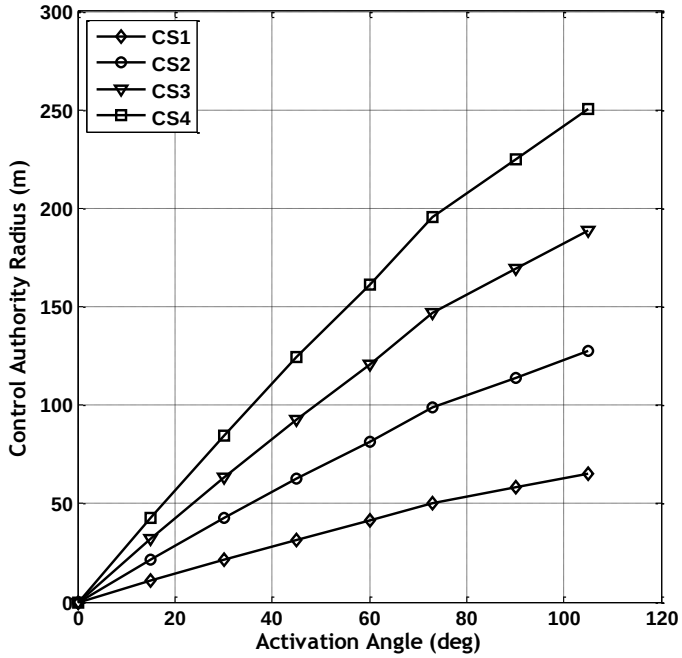

Figure 19. Trade study: effect of varied activation angle (δ) on full control authority with nominal conditions: t_a = 1.0 sec and Ma_i = 3.0.

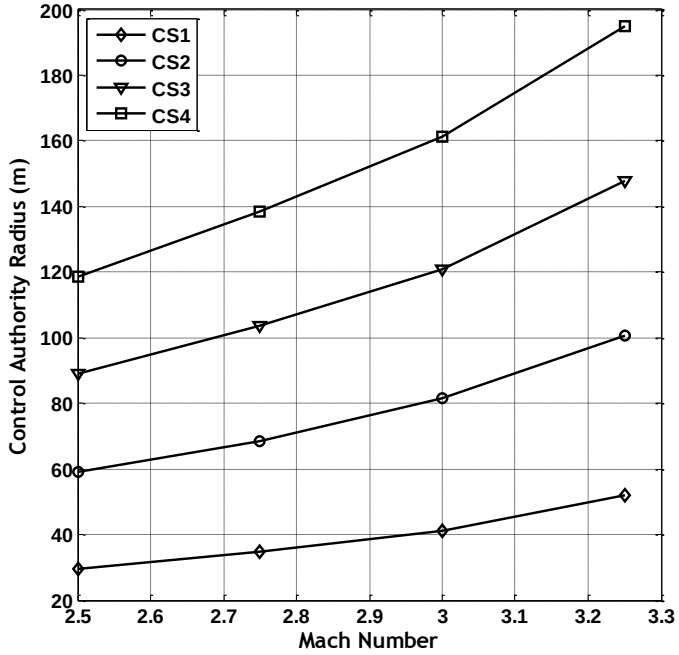

Figure 20. Trade study: effect of varied launch Mach number (Ma_i) on full control authority with nominal conditions: t_a = 1.0 sec and δ = 60°.

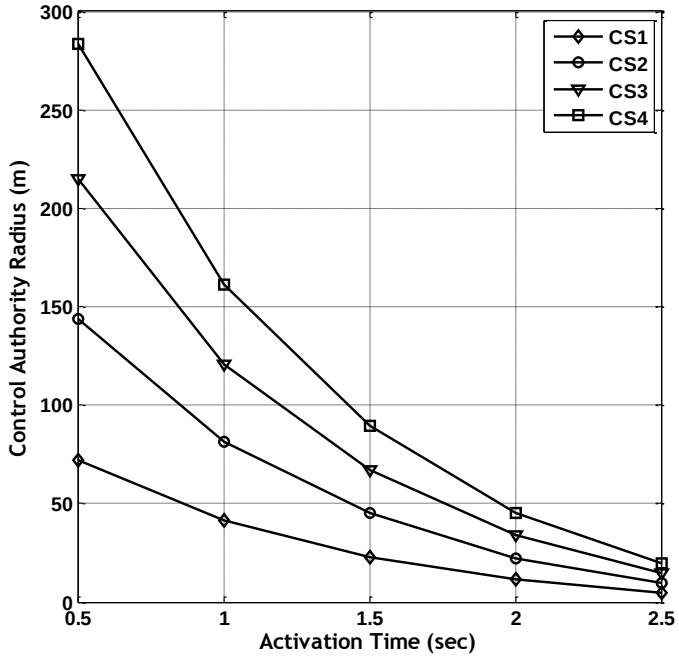

Figure 21. Trade study: effect of varied control system activation time (t_a) on full control authority under nominal conditions: δ = 60° and Ma_i = 3.0.

D. Active Control Analysis

An active control system is next developed to demonstrate the capabilities of the micro spoiler control mechanism to overcome typical launch and in-flight errors. This controller was designed to track a user specified commanded ballistic trajectory through use of GPS and other onboard sensors to provide feedback of *x*, *y*, *z*, and ϕ for the entire flight. The algorithm illustrated in Figs. 22 uses the command trajectory to develop an inertial-fixed projectile error vector, which is reduced by a proportional-integral-derivative (PID) controller through variation of the roll angle activation window. The total projectile inertial trajectory error Γ and the error command angle γ are defined in Eqns. (10) and (11).

$$\Gamma = \sqrt{e_y{}^2 + e_z{}^2} \tag{10}$$

$$\gamma = \tan^{-1}\left(\frac{e_z}{e_y}\right) \tag{11}$$

The error command angle and roll angle activation window are then input into the model prediction algorithm in Fig. 23, where γ provides an inertial direction for roll angle activation and δ specifies a neighborhood about γ for activation. The chosen command trajectory consisted of 30 discrete points to be linearly interpolated by the controller during flight and was generated by the nominal initial conditions previously used. Next, the following perturbed initial conditions were used for controlled and uncontrolled trajectories: x = 0.0 ft, y = 0.0 ft, z = -10.0 ft, ϕ = 0.0 rad, θ = 0.018 rad, ψ = 0.01 rad, u = 3360 ft/s, v = -1.14 ft/s, w = 0.0 ft/s, p = 0.17 rad/s, q = -0.79 rad/s, and r = 0.73 rad/s. For the controlled case, the roll angle activation window was limited to a maximum value of δ_{max} = 90.0 deg. Also, t_a = 1.0 sec, K_P = 0.261, K_I = 0.00154, and K_D = 0.0675.

Figs. 24-29 show the performance of the controlled projectile. Figs. 24 and 25 demonstrate the controlled projectile's ability to quickly converge to the command trajectory soon after activation. Note that the uncontrolled case misses the target (considered to be impact point of the commanded trajectory) by -3.1898 m in altitude and 30.7401 m in deflection, while the controlled case only misses the target by approximately 0.6217 m in altitude and 0.2373 m in deflection.

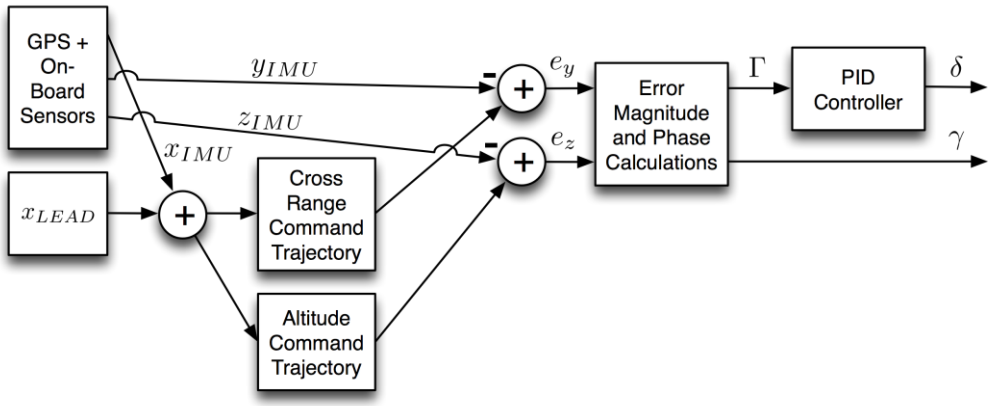

Figure 22. Control System Logic

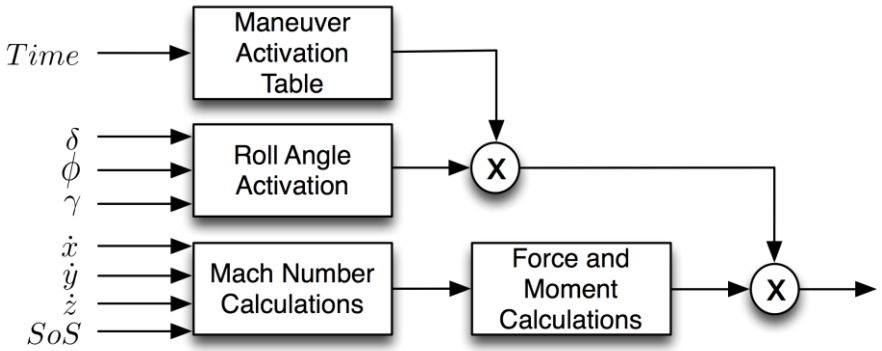

Figure 23. Micro Spoiler Logic

Fig. 26 shows that the total projectile angle of attack reaches a maximum value of 7.77 deg upon control maneuver activation but then quickly drops down below 3.0 deg within 1.0 sec. Fig. 27 shows variation in the error command angle after control maneuver activation. At first this angle is stays level at approximately 180.0 deg and then steadily descends. This implies that, once the controller is activated, the projectile turns left to approach the command trajectory and then starts to spiral about it in a clockwise manner, as it seeks the command trajectory. Fig. 28 shows that the total inertial error is rapidly reduced from 10.28 m to approximately 0.56 m after control maneuver activation and then levels off. This suggests that once the projectile has 'snapped' to the command trajectory and has begun to spiral about it, it does so at a nearly constant radius of 0.56 m. Fig. 29 shows the variation of the roll angle activation window after control maneuver activation, which is initially constant, since maximum control authority is needed, and then reduces down to around 30.0 deg.

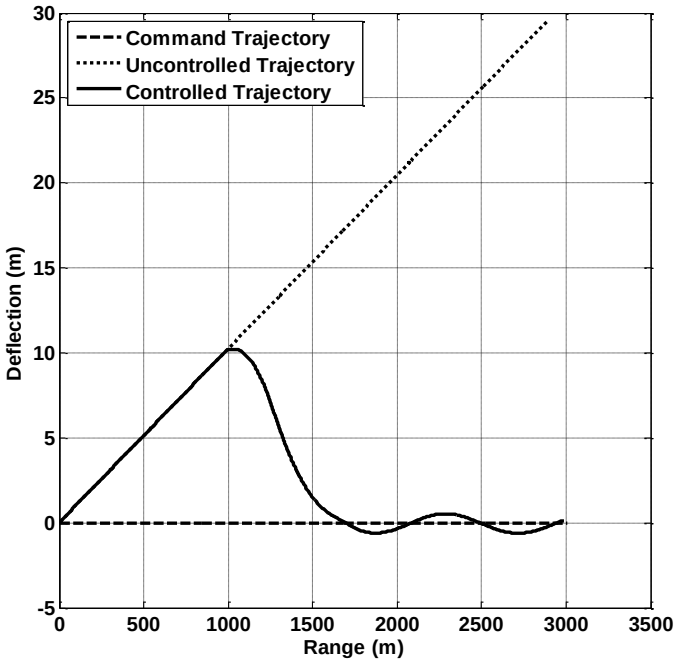

Figure 24. Deflection vs Range.

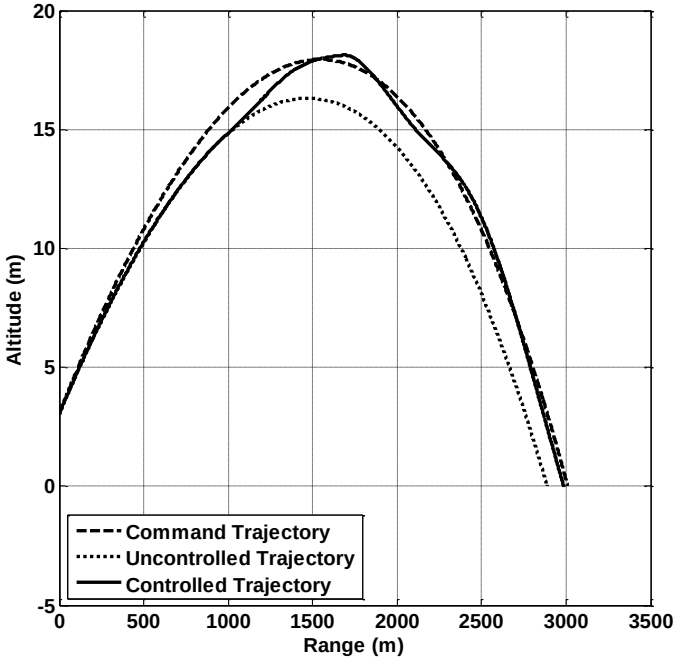

Figure 25. Altitude vs Range.

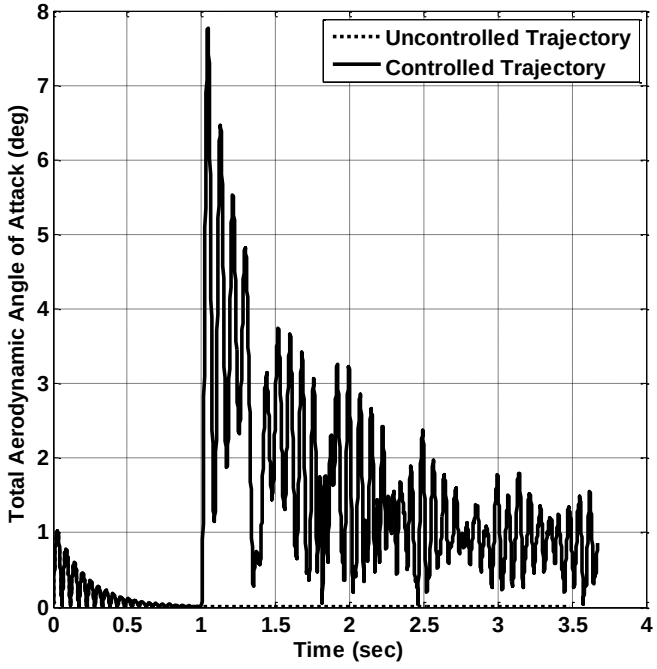

Figure 26. Angle of Attack vs Time.

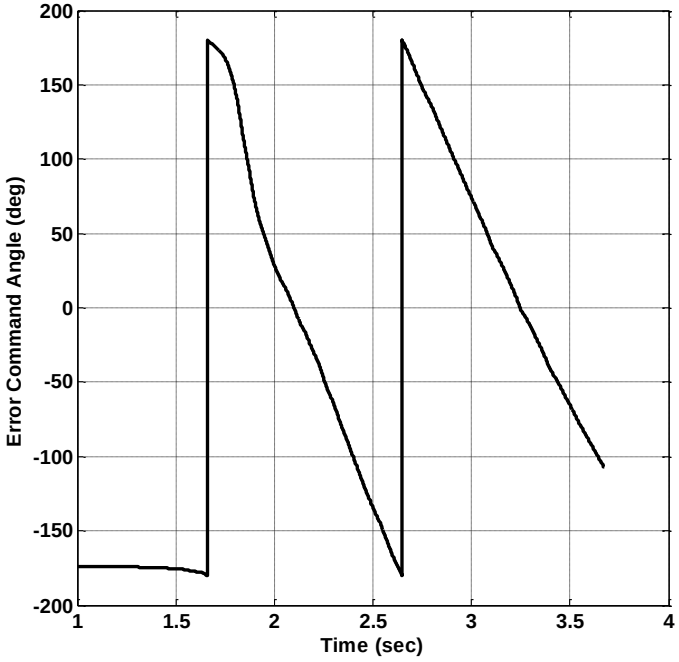

Figure 27. Error Command Angle vs Time after controller activation.

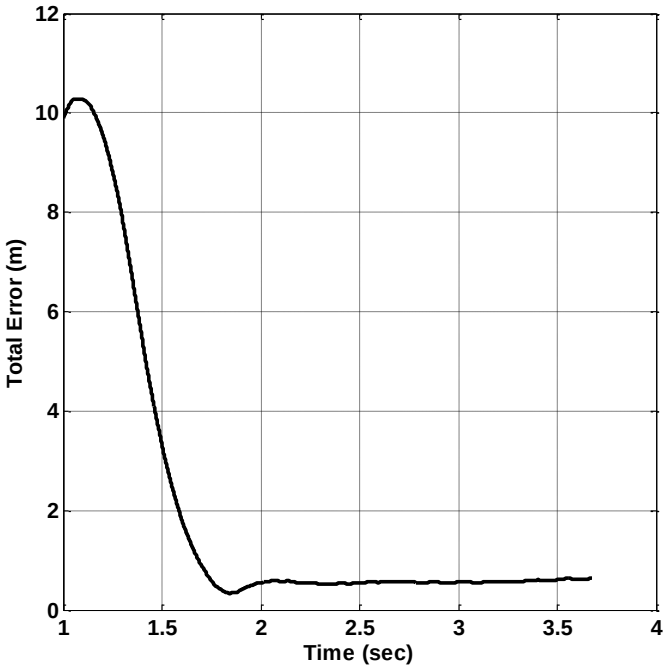

Figure 28. Total Error vs Time after controller activation.

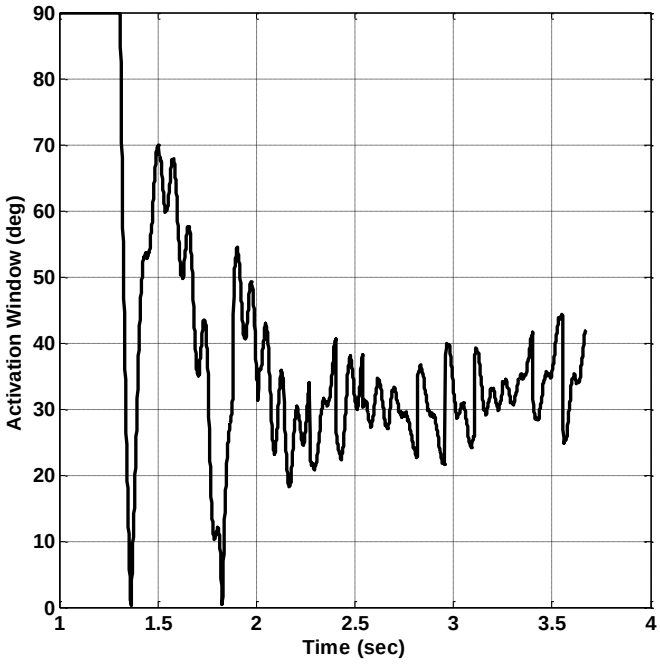

Figure 29. Roll Angle Activation Window vs Time after controller activation.

E. Dispersion Analysis

Monte Carlo dispersion cases were computed to demonstrate the performance of the control system with perturbed initial conditions (tip-off effects) and projectile mass/inertial property uncertainty. To simulate tip-off effects, initial states were perturbed from the nominal conditions which include initial pitch angle, initial yaw angle, initial muzzle velocity, initial crossing velocities in the *y* and *z* directions, initial roll rate, initial pitch rate, and initial yaw rate. The standard deviations for these values are 0.01 rad, 0.01 rad , 3.0 ft/s, 1.0 ft/s, 1.0 ft/s, 0.15 rad/s, 0.7 rad/s, and 0.7 rad/s respectively. To simulate variability in projectile weight, diameter, stationline center of gravity, moment of inertias about the *x*, *y*, and *z* body axes. Standard deviations for these parameters are 0.0837 lbf, 0.000052 ft, 0.00053 ft, 0.000000268 slugs-ft^2, 0.0000189 slugs-ft^2, and 0.0000189 slugs-ft^2 respectively.

Figs. 30 and 31 show the impact point results in a vertical plane at a range of 3.0 km for the uncontrolled and controlled dispersion cases. As observed, implementation of the micro spoiler control system causes a 97.86% reduction in the Circular Error Probable (CEP) - from 37.80 m (uncontrolled) down to 0.81 m (controlled). Note that the CEP was calculated about the mean impact values for each case. These results indicate that the micro spoiler smart projectile control mechanism is capable of reducing trajectory tracking errors down to sensor accuracy.

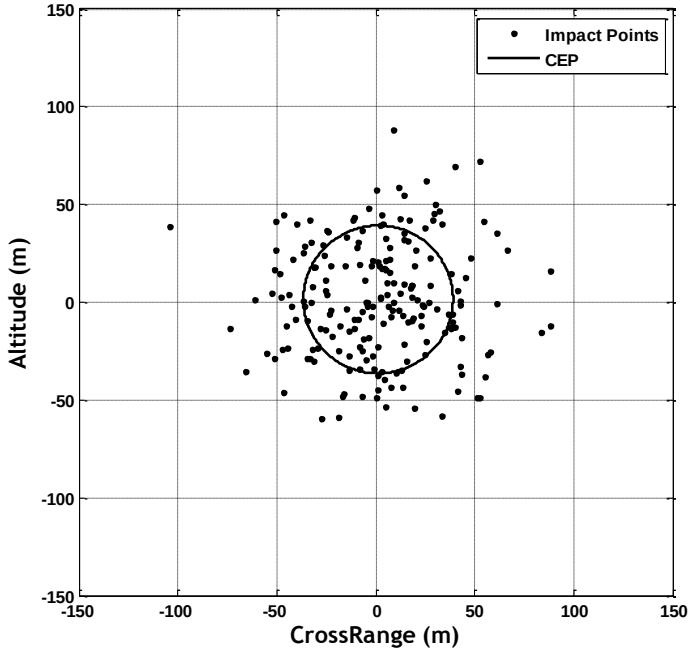

Figure 30. Monte Carlo dispersion spread and CEP for an uncontrolled projectile with variation in tip-off and projectile properties at an impact range of 3.0 km.

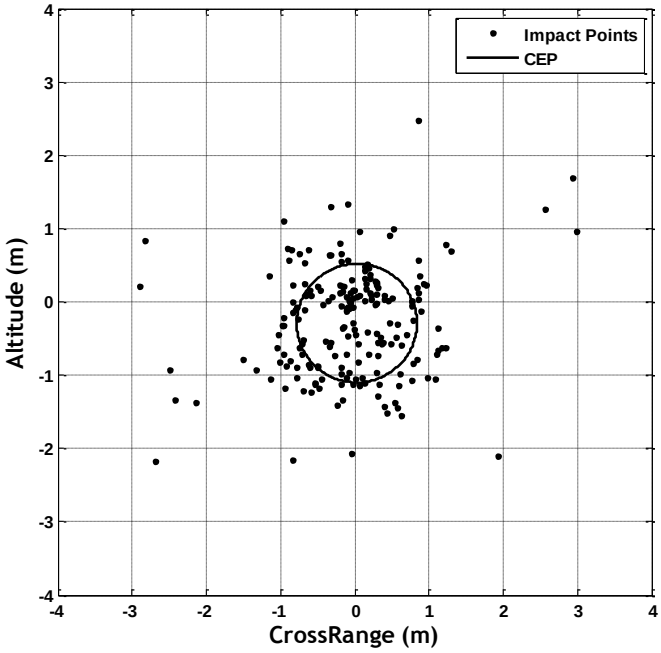

Figure 32. Monte Carlo dispersion spread and CEP for a controlled projectile with variation in tip-off and projectile properties at an impact range of 3.0 km.

V. Conclusions

This research indicates that micro spoiler implementation for active control of finned projectile in supersonic flight is a viable physical control mechanism that provides high maneuverability to the round. Control authority is linearly increased with the number of micro spoilers. Increasing the roll angle activation window also increases control authority but a point of diminishing return is reached beyond an angle of 110.0 deg. Increasing projectile launch muzzle velocity and decreasing control system activation time are also observed to have positive effects on control authority. The PID controlled dispersion results show that the micro spoiler mechanism is capable of reducing error down to sensor error, as nearly a 98% reduction in mean impact CEP is observed. The conclusions of this study are reached using 6-degree-of-freedom flight dynamic simulation to generate fly outs, with micro spoiler aerodynamic loads provided by computational fluid dynamics modeling.

VI. References

[1]Rogers, J., Costello, M., "Control Authority of a Projectile Equipped with a Controllable Internal Translating Mass", AIAA Paper 2008-6492, *AIAA Atmospheric Flight Mechanics Conference*, August 2007, Hilton Head, South Carolina.

[2]Richardson, D., "Summoning the Fire", Armada International, 27(1), p. 10, 2003.

[3]Gander, T. J., "Artillery On Target—Trajectory Correctable Munitions", Armada International, 27(2), p. 70, 2003.

[4]Massey, K. C., McMichael, J., Warnock, T., Hay, F., "Mechanical Actuators for Guidance of a Supersonic Projectile", AIAA Paper 2005-4970, *AIAA Applied Aerodynamics Conference*, June 2005, Toronto, Ontario Canada.

[5]Massey, K. C., Guthrie, K. B., "Optimized Guidance of a Supersonic Projectile Using Pin Based Actuators", AIAA Paper 2005-4966, *AIAA Applied Aerodynamics Conference*, June 2005, Toronto, Ontario Canada.

[6]Massey, K. C., Silton, Sidra I., "Testing the Maneuvering Performance of a Mach 4 Projectile", AIAA Paper 2006-3649, *AIAA Applied Aerodynamics Conference*, June 2006, San Francisco, California.

[7]Bell, M., Watterson, J. K., Lisk, D., "A Numerical Study into a Local Protuberance Interaction with a Fin on a Supersonic Projectile", AIAA Paper 2009-1092, *47th AIAA Aerospace Sciences Meeting Including The New Horizons Forum and Aerospace Exposition*, 5-8 January 2009, Orlando, Florida.

[8]McCoy, R. L., *Modern Exterior Ballistics*, Schiffer Publishing Ltd., Atglen, PA, 1999.

[9]Murphy, C. H., 1963, "Free Flight Motion of Symmetric Missiles", U.S. Army Ballistic Research Laboratories, BRL Report No. 1216.

[10]Costello M., Anderson D., "Effect of Internal Mass Unbalance on the Terminal Accuracy and Stability of a Projectile", AIAA Paper 1996, *AIAA Flight Mechanics Conference*, San Diego, California, 1996.

[11]Dupuis, A. and Hathaway, W., "Aeroballistic Range and Wind Tunnel Tests of the Basic finner Reference Projectile from Subsonic to High Supersonic Velocities", DREV-TM-136, October 2002.

[12]Carlucci, D., Jacobson, S., *Ballistics: Theory and Design of Guns and Ammunition*, CRC Press, Boca Raton, Florida, 2008.